Photouncaging Nanoparticles for MRI and Fluorescence Imaging *in Vitro* and *in Vivo*

Edakkattuparambil S. Shibu,[†] Kenji Ono,[‡] Sakiko Sugino,[†] Ayami Nishioka,[§] Akikazu Yasuda,[⊥] Yasushi Shigeri,[⊥] Shin-ichi Wakida,[†] Makoto Sawada,[‡] and Vasudevanpillai Biju[†,∥,*]

[†]Health Research Institute, National Institute of Advanced Industrial Science and Technology (AIST), Takamatsu, Kagawa 761-0395, Japan, [‡]Research Institute of Environmental Medicine, Nagoya University, Nagoya 464-8601, Japan, [§]Faculty of Engineering, Kagawa University, 2217-20, Takamatsu, Kagawa 761-0395, Japan, [⊥]Health Research Institute, National Institute of Advanced Industrial Science and Technology (AIST), 1-8-31 Midorigaoka, Ikeda, Osaka 563-8577, Japan, and [∥]PRESTO, Japan Science and Technology Agency, Tokyo 332-0012, Japan

ABSTRACT Multimodal and multifunctional nanomaterials are promising candidates for bioimaging and therapeutic applications in the nanomedicine settings. Here we report the preparation of photouncaging nanoparticles with fluorescence and magnetic modalities and evaluation of their potentials for *in vitro* and *in vivo* bioimaging. Photoactivation of such bimodal nanoparticles prepared using photouncaging ligands, CdSe/ZnS quantum dots, and super paramagnetic iron oxide nanoparticles results in the systematic uncaging of the particles, which is correlated with continuous changes in the absorption, mass and NMR spectra of the ligands. Fluorescence and magnetic components of the bimodal nanoparticles are characterized using scanning electron microscopy (SEM), transmission electron microscopy (TEM), and elemental analyses using energy dispersive X-ray (EDX) spectroscopy and X-ray photoelectron spectroscopy (XPS). Bioconjugation of the nanoparticles with peptide hormones renders them with biocompatibility and efficient intracellular transport as seen in the fluorescence and MRI images of mouse melanoma cells (B16) or human lung epithelial adenocarcinoma cells (H1650). Biocompatibility of the nanoparticles is evaluated using MTT cytotoxicity assays, which show cell viability over 90%. Further, we combine MRI and NIR fluorescence imaging in C57BL/6 (B6) mice subcutaneously or intravenously injected with the photouncaging nanoparticles and follow the *in vivo* fate of the nanoparticles. Interestingly, the intravenously injected nanoparticles initially accumulate in the liver within 30 min post injection and subsequently clear by the renal excretion within 48 h as seen in the time-dependent MRI and fluorescence images of the liver, urinary bladder, and urine samples. Photouncaging ligands such as the ones reported in this article are promising candidates for not only the site-specific delivery of nanomaterials-based contrast agents and drugs but also the systematic uncaging and renal clearance of nanomaterials after the desired *in vivo* application.

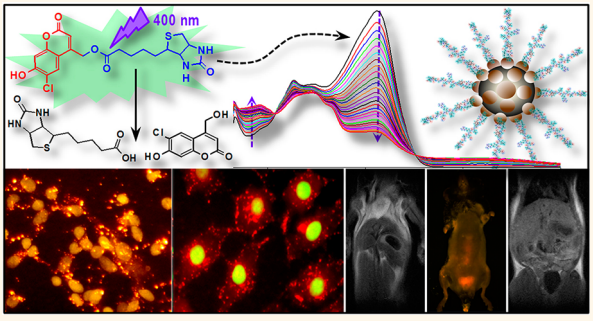

KEYWORDS: quantum dots · fluorescence · photouncaging · iron oxide · multimodal nanoparticles · MRI

Multimodal and multifunctional nanoparticles receive considerable attention in the recent past owing to their growing applications such as multiplexed detections both *in vitro* and *in vivo*.[1] Combination of fluorescence and magnetic modalities in a single nanometer-scale probe enables one to develop smart bimodal nanomaterials, which find applications in bioimaging,[2] photothermal[3] and photodynamic therapies,[4] magnetic separation,[5] rapid and dynamic intracellular patterning,[6] detection and isolation of multiple tumors,[7] and gene and drug delivery.[8,9] Fluorescent probes other than organic dyes used in the construction of multimodal nanoparticles (NPs) include semiconductor quantum dots (QDs),[10−12] lanthanide complexes,[2] and upconversion NPs.[13,14] Among these materials, QDs receive considerable attention owing to their unique properties such as broad absorption and narrow emission bands, large molar extinction coefficient, and exceptional photostability.[15−17] The different magnetic probes included in multimodal imaging probes are derived from iron oxide,[18] FePt alloy,[19] cobalt,[20] cobalt−ferrate alloy,[21] ferritin[10] and gadolinium chelates.[4] However, the exact machinery for the degradation of such NPs and their removal from biological systems after imaging and therapy remains mostly unknown. To look into this

* Address correspondence to v.biju@aist.go.jp.

Received for review July 9, 2013 and accepted October 1, 2013.

Published online October 01, 2013
10.1021/nn4043699

issue, we develop photouncaging bimodal nanoparticles (PUNPs) in which fluorescent and magnetic components are caged by photouncaging ligands, and evaluate the photouncaging properties of the ligands and PUNPs. Here, photouncaging ligands refer to those which could be easily degraded by applying light without involving any chemical reagent. Recently, photouncaging molecules find interesting applications in different aspects of chemical biology such as spatially and temporally controlled delivery of drugs and biomolecules.[22−24] Among the various photouncaging molecules known so far, coumarinylmethylesters[25−27] are extensively investigated due to their efficient photolysis.

Common techniques for the preparation of multimodal NPs include co-encapsulation,[28] epitaxial heterogeneous growth,[29] precipitation,[30] covalent conjugation[31] and electrostatic assembly.[32] Among these methods, covalent conjugation and electrostatic assembly of contrast agents or drugs in silica NPs, semiconductor QDs, gold NPs, liposomes, polymer NPs, carbon nanotube, fullerene or graphene are widely appreciated.[20,31,33−42] Biotin derivatives prepared using coumarinylmethyl ester allow us to assemble multiple fluorophores on the surface of magnetic NPs and obtain fluorescent and magnetic PUNPs. First, we demonstrate the synthesis of two novel photouncaging biotin derivatives, namely, coumarinylmethyl biotin ester (**3**) and coumarinylmethyl bis-biotin ester (**5**), and then extend to the fabrication of PUNP composed CdSe/ZnS QDs and Fe_3O_4 NPs using **5**, which is characterized using scanning electron microscopy (SEM), transmission electron microscopy (TEM), energy dispersive X-ray (EDX) and X-ray photoelectron spectroscopy (XPS) methods. Further, PUNPs are conjugated with a peptide hormone allatostatin I, which facilitates intracellular delivery of PUNPs in mammalian cells. Photouncaging of **3**, **5** and PUNP is investigated using time-dependent UV−vis absorption spectroscopy, nuclear magnetic resonance (NMR) spectroscopy, and matrix-assisted laser desorption ionization (MALDI) time-of-flight (TOF) mass spectroscopy. The formation of coumarinylmethyl alcohol and biotin during the photoactivation of **3** or **5** confirms the photouncaging steps. Evaluation of the cytotoxic effects of **3**, **5**, peptide-labeled PUNP and photouncaged products in human lung epithelial adenocarcinoma cells (H1650) and mouse melanoma cells (B16) using 3-(4,5-dimethylthiazol-2-yl)-2,5-diphenyltetrazolium bromide (MTT) assays shows over 90% viability, which indicates the active metabolism of cells labeled with PUNPs or its components. Finally, we use peptide-conjugated PUNP as an efficient contrast agent for MRI and fluorescence imaging of B16 cells and C57BL/6 (B6) mice. The enhanced magnetic and fluorescence contrasts collected from cells treated with or mice injected with PUNP confirm the bimodal nature of the NP. Further, MRI and fluorescence images of the liver, urinary bladder and urine samples collected from the mice at different time intervals are recorded and analyzed for validating the renal clearance of PUNPs.

RESULTS AND DISCUSSION

Figure 1A and B shows steps involved in the synthesis of **3**, **5**, and PUNPs. Details of organic chemical reactions involved in the preparation of **3** and **5** and their characterization are given in the Experimental Methods section. During the fabrication of PUNPs, concentrations of streptavidin-functionalized Fe_3O_4 NPs and **5** are set at 1:100 ratio, such that streptavidin pockets in Fe_3O_4 NPs are completely occupied by **5** and provide photouncaging biotin-functionalized Fe_3O_4 NPs. Here, the stepwise addition of Fe_3O_4 NPs to a large excess of **5** prevents any ligand-mediated aggregation of Fe_3O_4 NPs. Free ligands are successively removed by dialysis against a membrane for 2 kDa. Subsequently, the biotinylated Fe_3O_4 NPs are added in five portions to streptavidin-functionalized QDs in 1:10 ratio, which assembles *ca.* 10 QDs on each Fe_3O_4 NPs through the photouncaging biotin ligand. Any QD left free in the reaction mixture is removed overnight by repeated magnetic separation using a bar magnet. Details of the preparation of PUNPs are given in the Experimental Methods section. Bright-field optical image (C), fluorescence image (D), and T_1- (E) and T_2-weighted (F) MRI taken for solutions of phosphate buffered saline (PBS) (i), CdSe/ZnS QDs (ii), Fe_3O_4 NPs (iii) and PUNPs (iv) are given in Figure 1C−F. The intense magnetic and fluorescence contrasts from PUNPs in addition to the integrated features of QDs, **5** and Fe_3O_4 NPs in the optical absorption and photoluminescence spectra (Supporting Information, Figure S1) show the bimodal nature of PUNPs. The MR and fluorescence contrasts are not due to the presence of free Fe_3O_4 and QDs, which is confirmed by obtaining morphology of PUNPs using SEM. The size-distribution and shape of PUNPs are shown in Figure 1G. PUNP is further characterized by recording and analyzing STEM micrographs (Figure 1H), elemental maps (Figure 1I−L), EDX spectrum (Figure 1M), and XPS (Figure S2). The morphology and the elemental composition (Fe, O, Cd, and Se) analyzed using EDX and XPS confirm the structure and bimodal nature of PUNPs.

To evaluate the photouncaging nature of **3**, **5** and PUNP, we have studied the kinetics of photouncaging using time-dependent UV−vis absorption spectroscopy, ^{1}H NMR spectroscopy, and MALDI-TOF mass spectroscopy. Schematic presentation of photouncaging and the underlying mechanism are shown in Figure 2A. First, 1 μM solution of **3** in DMF:water (10:1) mixture is illuminated with either 400 nm light from a Xe lamp or 400 nm laser (7 mW/cm^2), and the UV−vis absorption spectra of the solution are recorded at equal time intervals. As seen in Figure 2B, a continuous drop in the absorbance *ca.* 410 nm and evolution of a new

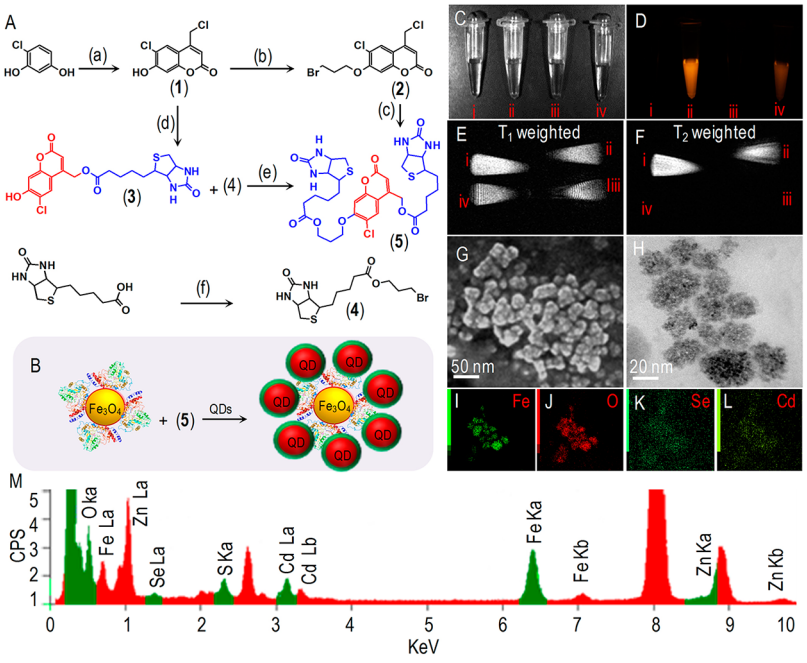

Figure 1. Synthesis and characterization of PUNP. (A and B) Scheme for the synthesis of (A) 3 and 5, and (B) PUNP: (a) ethyl-4-chloroacetoacetate, methanesulfonic acid, RT, 2 h; (b) 1,3-dibromopropane, DBU, 150 °C; (c) K_2CO_3, DMF, 100 °C; (d) biotin, DBU, dry ethanol, 135 °C; (e) K_2CO_3, DMF, 150 °C; (f) 1,3 dibromopropane, DBU, acetonitrile, 90 °C. (C) Optical image, (D) photoluminescence image, and (E) T_1-weighted MRI and (F) T_2-weighted MRI of solutions of (i) PBS, (ii) QD, (iii) Fe_3O_4 NP and (iv) PUNP. (G) FESEM image, (H) STEM image, (I−L) elemental maps, and (M) EDX spectrum of PUNP.

band *ca.* 275 nm through an isosbestic point shows the photouncaging reaction. Conversely, the absorption spectrum of a control sample kept in the dark remains essentially intact (Figure 2C). Plots of absorbencies *vs* time at 410 and 275 nm during the course of photouncaging are shown in the inset of Figure 2B, which follow the first order kinetics. Using the number of reacted molecules, which is calculated from the molar extinction coefficient and the difference in the absorbencies, and the number of absorbed photons, which is calculated from the excitation laser intensity and photon energy, we estimate the quantum efficiency of photouncaging reaction at ~4.8%. To further evaluate the photouncaging reaction, we recorded and analyzed the MALDI-TOF mass spectra of **3** before (Figure 2D) and after (Figure 2E) photoirradiation. Samples for MALDI-TOF mass analyses were loaded in the standard α-cyano-4-hydroxycinnamic acid matrix. As expected, the molecular peak of **3** (m/z = 453) in a photoactivated sample is completely disappeared, which is associated with the formation of the photoproducts shown in Figure 2A. These changes to the mass spectra are in good agreement with the photouncaging process as seen in the absorption spectra (Figure 2B).

The photouncaging nature of allylic ester and the formation of primary alcohol make it possible for us to further evaluate the photouncaging reaction by following the time-dependent ^{1}H NMR spectra of **3** dissolved in deuterated DMSO and exposed to 400 nm laser (Figure 2F). The downfield shift of the broad doublet at 5.33 ppm due to coumarinylmethyl protons (Figure 2H) and appearance of a broad triplet at 6.24 ppm (Figure 2G) due to the spatial coupling of allylic proton with the newly formed hydroxymethyl group confirm the photouncaging reaction. More interestingly, the photouncaged sample in the NMR tube exposed to UV light shows white light emission, which is resolved into individual colors using band-pass filters as seen in Figure 2I. We attribute the white light emission to aggregation and the formation of excimer of hydroxymethylcoumarin, which is facilitated by its simple molecular structure when compared with the biotinylated caged form **3**. Likewise, the photouncaging of **5** is characterized using time-dependent UV−vis absorption spectroscopy (Supporting Information). The photouncaging of such allylic esters follow the photo S_N1 reaction, which is the solvent-assisted photoheterolysis from the lowest excited singlet state (S_1) *via* the singlet ion pair state. In general, photoactivated allylic esters of coumarin relax first to the S_1 state (^{1}[CM-A]*) followed by deactivation *via* radiative relaxation, nonradiative relaxation, and heterolytic bond cleavage into the singlet ion pair state (^{1}[CM^+ A^-]). The ion pair decays by either charge recombination to the ground state (CM-A) or charge separation to carbocation (CM^+) and carboxylate ion (A^-). Finally, reaction of the carbocation with water molecule and subsequent deprotonation results in the formation of alcohol. On the basis of the formation of photouncaged coumarin alcohols and biotin as seen in NMR and mass spectra, we attribute that the photouncaging of **3** and **5** follows the photo S_N1 reaction.

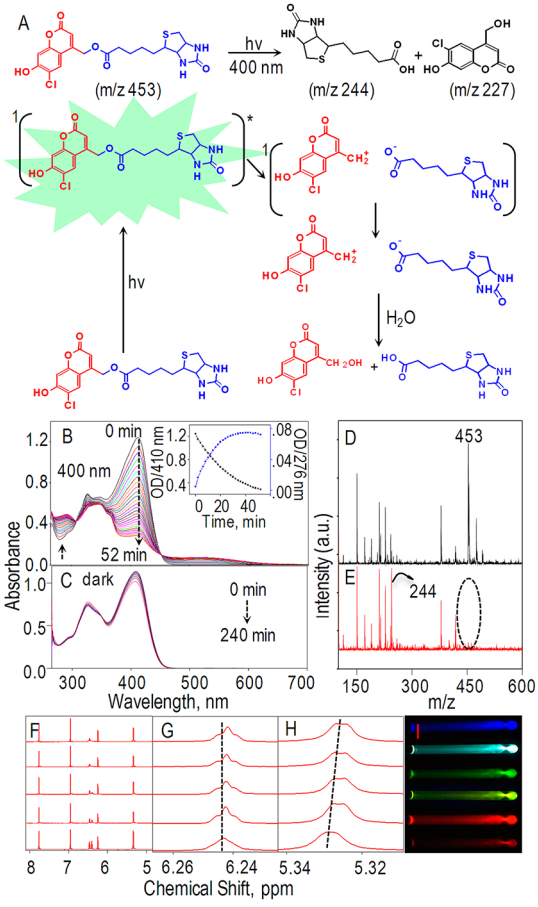

Figure 2. Photouncaging. (A) Scheme for SN[1] photouncaging reaction of substituted coumarins under 400 nm excitation; (B and C) temporal evolution of UV−vis absorption spectra of 3 under (B) photoactivation at 400 nm or (C) dark. Inset: the kinetics of photouncaging reaction. (D and E) MALDI-TOF mass spectra of 3 (D) before and (E) after photouncaging. (F) ^{1}H NMR spectra of 3 dissolved in DMSO-d_6 (bottom) before photoirradiation at 400 nm and (bottom to top) with progressive irradiation for 5 min each. (G and H) Enlarged ^{1}H NMR spectra of (G) allylic proton and (H) coumarinylmethyl protons. (I) Fluorescence images of uncaged products excited with UV light and collected through different band-pass filters.

To evaluate the photouncaging of PUNP, we have recorded and analyzed the FESEM images of PUNP after illumining with 340 nm light from a Xe lamp. Interestingly, we observed fragmented NPs rather than larger spheroid nanostructures in the photoirradiated samples. The photouncaging nature of **3** and **5** and the formation of small nanostructures in photoirradiated PUNP samples indicate the successful photouncaging of PUNPs. To evaluate the potentials of PUNPs and the ligands for biological applications under NIR excitation, we have obtained the two-photon action cross section of **3** using the equation, $\delta_s = \delta_r[S_s\Phi_r\phi_r c_r/S_r\Phi_s\phi_s c_s]$.[43] The subscript s and r stand for sample and reference. S is the signal collected by a PMT detector, Φ is the fluorescence quantum yield, ϕ is the overall fluorescence collection efficiency of the experimental apparatus, and c is the number density of the molecules in the solution. The calculated two-photon action cross section of **3** is 16 GM units, which is comparable to the cross section (~21 GM) of the standard rhodamine B.[44]

The combination of MRI and fluorescence contrast agents in a single entity allows us to obtain combined MRI and fluorescence images *in vitro* and *in vivo*. At first, we tested the bimodal imaging and cytotoxic effects of PUNP in cultured human and mouse cells. We employed allatostatin I, a peptide hormone present in insects and crustacean, as the endocytosis machinery.[45−47] Allatostatin is biotinylated using 3-sulfo-*N*-hydroxysuccinimide ester of biotin and subsequently conjugated to streptavidin moieties in PUNPs at 1:5 molar ratio (PUNP:allatostatin). Detailed procedures for the biotinylation of allatostatin and bioconjugation of PUNPs are given in the Experimental Methods section. Mouse melanoma cells (B16) cultured up to 60% confluence are incubated with a 5 μM solution of PUNP-allatostatin conjugate in Dulbecco's Modified Eagle Medium (DMEM) without phenol red or fetal bovine serum (FBS) for 1 h at 4 °C, and washed three times with PBS followed by treatment for 10 min with a 5 nM solution of the nucleus staining dye Syto 21. After the treatment, the cells are washed three times with PBS and the medium is exchanged with DMEM supplemented with 10% FBS. The intracellular delivery of PUNP in B16 cells is investigated using fluorescence microscopy. The excitation light used during imaging are 400 nm fs laser for Syto 21 and QDs and 532 nm cw laser for QD alone. Figure 3A shows the fluorescence image of B16 cells obtained by exciting at 400 nm and collecting the fluorescence signals through a 580 nm long-pass filter. Here, the nuclei of the cells appear orange due to the fluorescence tailing of the green fluorescent Syto 21, and the red fluorescence in the cytoplasm is contributed by the intracellular PUNPs. Figure 3B is an overlay image of the images obtained by exciting at 400 nm and collecting the fluorescence signals through a 510−550 nm band-pass filter for Syto 21 and a 580 nm long-pass filter for PUNPs. Figure 3C is an overlay of optical transmission and fluorescence images, which clearly indicates endocytosis of PUNPs in B16 cells. Large area fluorescence images of cells are given in the Supporting Information. We further compared the efficiency of allatostatin-mediated endocytosis of PUNPs with that of EGF-mediated endocytosis of QDs. Figure 3D is the overlaid fluorescence images of human lung epithelial adenocarcinoma cells (H1650) treated with QD-EGF conjugate. In Figure 3D, the nuclei are stained green using Syto 21 (Figure 3E), and the red fluorescence in the cytoplasm comes from QDs. Figure 3F is an overlay of optical transmission and fluorescence images, which clearly indicates an efficient intracellular delivery of QD-EGF conjugates in H1650 cells. On the other hand, EGF conjugates of QDs or PUNPs are not efficiently delivered in B16 cells,

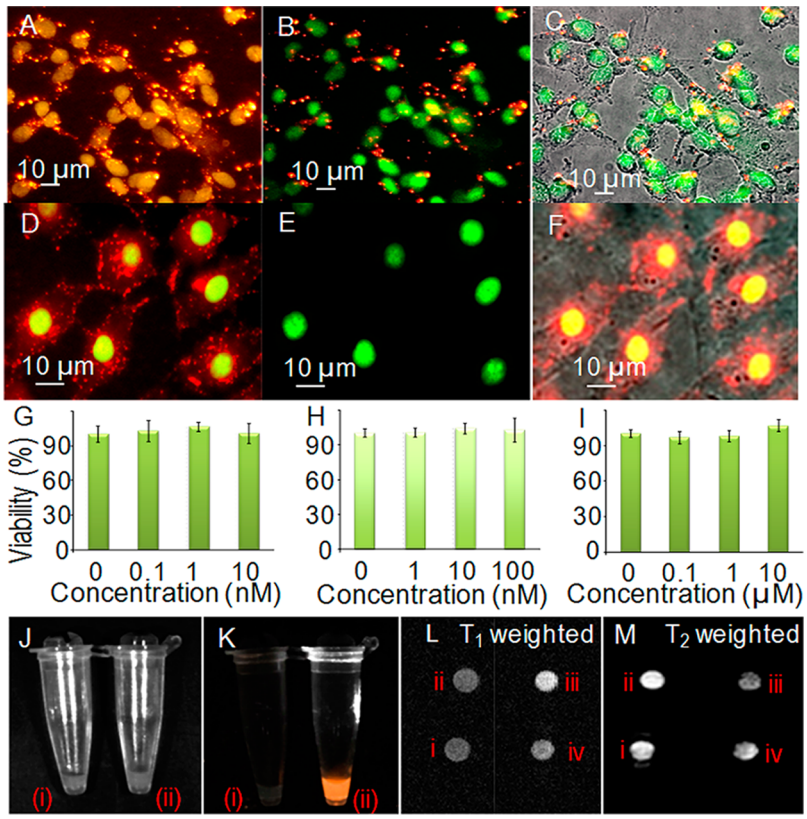

Figure 3. Intracellular delivery and MTT cytotoxicity assay. (A–C) Fluorescence and overlay images of B16 cells labeled with PUNP-allatostatin conjugates and Syto 21 dye (nucleus). (D–F) Fluorescence and overlay images of H1650 cells labeled with QD-EGF conjugates and Syto 21 dye (nucleus). (G–I) MTT assay histograms for H1650 cells treated with (G) CdSe/ZnS QD, (H) Fe_3O_4 NP and (I) PUNP. (J) Optical transmission and (K) fluorescence images of B16 cell pellets (i) without or (ii) with labeling using PUNP–allatostatin conjugate. (L) T_1- and (M) T_2-weighted MRI of (i) a 20 nM solution of Fe_3O_4 NP, (ii) PBS, (iii) B16 cells labeled with PUNP–allatostatin conjugate and (iv) unlabeled cells.

which we attribute to the poor expression of EGFR receptors in B16 cells. To address the toxicity of QDs, Fe_3O_4 NPs, PUNPs and the photouncaging products, we have measured the metabolic activities of cell using MTT cytotoxicity assay. Detailed procedure of MTT assay is given in the Experimental Methods section. Here, the MTT assays of CdSe/ZnS QDs (Figure 3G), Fe_3O_4 NPs (Figure 3H), PUNPs (Figure 3I), **3** (Supporting Information), **5** (Supporting Information) and the photoproducts (Supporting Information) show over 90% cell viability under a range of concentrations, which is indicative of the active metabolism of cells labeled with PUNP or its constituents. Nevertheless, impairment of cell membrane and other vital biological structures by PUNP are not completely reflected in the MTT assay.

To evaluate the potentials of PUNP to be an *in vitro* bimodal imaging probe, we have recorded MRI and fluorescence images of cells labeled with PUNP-allatostatin conjugate. First, B16 cells cultured up to 90% confluence are incubated with 5 nM solution of the conjugate in DMEM without phenol red or FBS for 1 h at 4 °C as described above. The cells are then washed three times with PBS, harvested using trypsin, further washed three times with DMEM supplemented with FBS, and the labeled cells are collected by centrifugation. Figure 3J and K shows bright-field and fluorescence images of B16 cell pellets (i) without and (ii) with labeling using PUNP-allatostatin conjugates. Fluorescence images of individual cells (Figure 3A) and cell pellet (Figure 3K) confirm the fluorescence modality provided by PUNPs. Figure 3L and M shows T_1- and T_2-weighted MRI of Fe_3O_4 NPs, PBS, and cell pellets labeled with and without PUNPs. The dark contrast of the labeled cells in T_2-weighted MRI is due to the contrast enhancement provided by PUNPs under the longer echo time (T_E) and repetition time (T_R) in the T_2 mode. The dark MRI contrast provided by PUNP is promising for discriminating labeled cells from unlabeled cells, lipid, water and fat which provide bright contrast.

To evaluate the potentials of PUNP for *in vivo* bimodal imaging, we have recorded the MRI and fluorescence images of C57BL/6 (B6) mice subcutaneously or intravenously injected with PUNPs. At First, anesthesia was administered intraperitoneally by using pentobarbital sodium (40 mg kg^{-1}).

Following sedation, 10 nM solutions of QDs, Fe_3O_4 NPs, PUNPs and PBS are subcutaneously injected at different places in a B6 mouse as seen in Figure 4A and B. *In vivo* fluorescence images are collected immediately

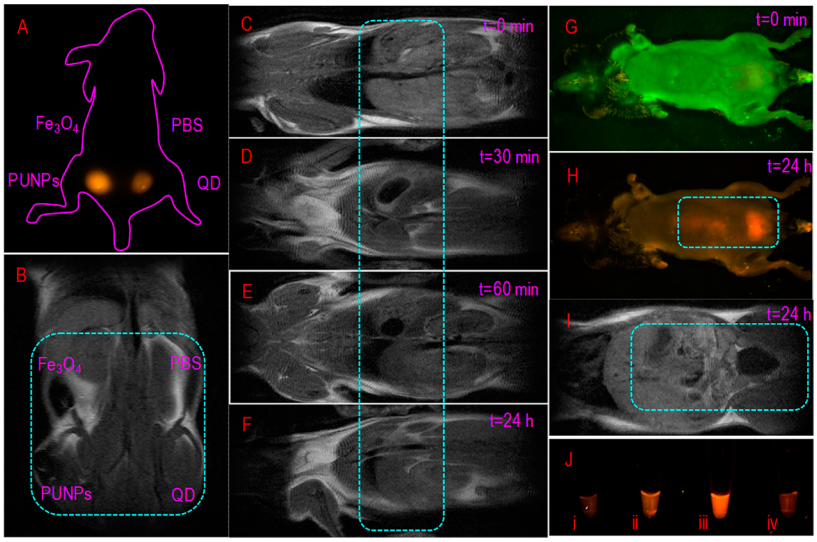

Figure 4. *In vivo* **MRI and fluorescence imaging. (A) Fluorescence image, and (B) T_1-weighted MRI of a B6 mouse subcutaneously injected with PBS, QD, Fe_3O_4 NP, and PUNP. (C–F) T_1-weighted MRI. (G) Fluorescence image of a mouse before injection, (H) fluorescence and (I) MRI images of the mouse 24 h after intravenous injection of PUNP. (J) Fluorescence images of urine samples collected from the mouse: (i) before injection of PUNP, and *ca.* (ii) 3 h, (iii) 24 h, and (iv) 48 h post injection.**

after the injection by exciting with band-pass filtered light (green-yellow light from a Xe lamp). Photographs of the mouse collected through a 580 nm long-pass filter show fluorescence signals at excellent signal-to-noise ratios from areas where QD (control) or PUNP was injected (Figure 4A). Similarly, T_1-weighted MRI of the mouse shows subcutaneous contrast enhancement at areas injected with Fe_3O_4 NP (control) or PUNP (Figure 4B). Further, to test the potentials of detecting fluorescence and MRI contrasts of PUNPs in deep buried tissues such as the liver, we injected PUNPs (10 nM, 250 μL) intravenously in a C57BL/6 (B6) mouse that is different from the one examined above, and obtained MRI and fluorescence images at different time intervals after the injection. T_1-weighted MRIs of the mouse obtained at $t = 0$ to $t = 24$ h as seen in Figure 4C–F show contrast enhancement in the liver. Interestingly, PUNP accumulated in the liver within 30 min post injection and subsequently cleared by the renal excretion within 24 h as seen in Figure 4D–F. The poor penetration of visible excitation light and the emitted fluorescence through tissues is one of the major challenges associated with *in vivo* fluorescence imaging. To address this issue, we have used PUNP composed of NIR-emitting QDs (QD_{705}) and Fe_3O_4 NPs. NIR fluorescence of PUNPs allows us to not only obtain enhanced fluorescence contrast *in vivo* (Figure 4H) but also follow the clearance of intravenously injected PUNPs from the body. MRI and fluorescence images of mice collected at different time intervals show initial (30–60 min) contrast enhancements in the liver (Figure 4D), decrease of the contrasts within 24 h (Figure 4F and H), and concomitant contrast enhancements in the urinary bladder (Figure 4H and I). The enhanced MRI and fluorescence contrasts of the bladder show renal clearance of PUNP within 48 h post injection. Further, we have collected urine samples from the mice before and at different time intervals after the intravenous injection of PUNPs. Urine sample collected *ca.* 24 h post injection shows enhanced fluorescence (Figure J; iii), which is consistent with the MRI and fluorescence contrast enhancement in the urinary bladder *ca.* 24 h post injection (Figure 4H and I). Further, the fluorescence of urine sample collected after 48 h show less fluorescence. The renal clearance of *ca.* 30 nm diameter PUNP though the anatomical and physiological barrier (<25 nm) provided the Bowman's capsule in the renal corpuscle suggests a possibility that the particles are separated into individual components by hepatocytes during the initial accumulation in the liver. In short, the NIR-fluorescence of QDs and the MRI contrast of Fe_3O_4 NPs in PUNP are useful for the combined *in vivo* fluorescence and MRI imaging and analyzing the clearance of intravenously injected NPs.

CONCLUSION

By using light as the innovative tool, we introduce a simple strategy for the fragmentation of photouncaging ligands that bond magnetic and fluorescent components in photouncaging nanoparticles. The photouncaging processes are elucidated by observing systematic changes in the absorption, mass and NMR spectra of the photouncaging ligands as well as the SEM image of the nanoparticles. Successively, the photouncaging nanoparticle is applied as bimodal contrast agent for the combined MRI and NIR fluorescence imaging of melanoma cells and B6 mice.

In vivo MRI and fluorescence images of B6 mice either subcutaneously or intravenously injected with the photouncaging nanoparticles show magentic and fluorescence contrast enhancements under the skin or in the liver. MRI and fluorescence images of the liver, urinary bladder and urine samples obtained at different time intervals show the renal clearance of the nanoparticles within 48 h. Photouncaging ligands such as the ones reported in this article boast great potentials for the fabrication of photocleavable tool boxes such as multimodal and multifunctional nanoparticles for bioimaging and cancer therapy.[48−52] Such photouncaging ligands facilitate not only the site-specific delivery of contrast agents and drugs, but also the systematic uncaging of nanoparticles into fragments and the subsequent renal clearance after the desired application. Although the penetration of excitation light into deep-burried tissues is limited, the strategy of photouncaging for the photocontrolled delivery and clearance of nanomaterials is promising for *in vivo* biological applications that involve light, such as fluorescence imaging, photothermal imaging, photoacoustic imaging, photothermal therapy, and photodynamic therapy.

EXPERIMENTAL METHODS

All the chemicals and solvents are analytical grade and used without further purification. CdSe/ZnS QDs (PL maximum ~655/705 nm) are obtained from Invitrogen Corporation and Fe_3O_4 NPs from NANOCS. 4-Chlororesorcinol, ethyl-4-chloroacetoacetate, methanesulfonic acid, biotin and 1,8-diazabicyclo[5.4.0]-7-undecene (DBU) are obtained from Sigma Aldrich. K_2CO_3 and 1,3-dibromopropane are obtained from Tokyo Chemical Industries.

^{1}H and ^{13}C NMR measurements are carried out in a JEOL 400 MHz spectrometer. MALDI/LDI-TOF mass measurements are carried out using a BRUKER Microflex spectrometer. Fluorescence images of labeled cells are acquired in an inverted optical microscope (Olympus IX70) equipped with a 40× objective lens, a 2.5× telescopic lens, band-pass/long-pass filters for QDs and Syto 21 dye, and an electron multiplying charge coupled device (EMCCD, Andor Technology) or a CCD camera (Olympus). Excitation light sources used for fluorescence imaging are 400 or 532 nm laser. FESEM images are acquired using a JSM-6700FZ (JEOL) microscope operating at 10 μA and 15 kV. MRI data are acquired using a small animal imaging MRI equipment (MR Technology, Inc., Tsukuba, Japan). Fluorescence images of B16 cell pellets and B6 mice are recorded using a Maestero small animal imaging system (Perkin-Elmer). MRI and fluorescence images of cell pellets and mice are analyzed using Maestro software (Cambridge Research & Instrumentation, Inc.) and Image-Pro Plus software (Roper Industries, Inc., Sarasota, FL).

Synthesis of 1. A mixture of 4-chlororesorcinol (14.4 g, 100 mmol) and ethyl-4-chloroacetoacetate (19.9 g, 120 mmol) dissolved in methanesulfonic acid (160 mL) is stirred for 4 h at room temperature and subsequently poured into ice-cold water with constant stirring for 1 h. The off-white precipitate formed is filtered, copiously washed with ice-cold water, and dried under reduced pressure to yield the desired product (22 g, 90%). ^{1}H NMR (400 MHz, DMSO-d_6) δ = 4.99 (s, 2H), 6.49 (s, 1H), 6.96 (s, 1H), 7.8 (s, 1H), 11.5 (s, 1H); ^{13}C NMR (100 MHz, DMSO-d_6) δ = 59.70, 104.30, 108, 111.90, 112.30, 117.30, 126, 153.89, 156.84, 160.63; FT-IR (ν_{max}) = 3297, 1702, 1611, 1553, 1504, 1430, 1399, 1342, 1291, 1170, 1138, 1068, 1036, 941, 891, 738, 643, 534 cm^{-1}; MALDI-TOF ($C_{10}H_6Cl_2O_3$), m/z = 245.

Synthesis of 2. A suspension of **1** (2.4 g, 9.8 mmol) prepared in 1,3-dibromopropane (10 mL, 98.95 mmol) by sonication is mixed with DBU (1.5 mL, 10.05 mmol) and heated at 150 °C for 30 min. The product is extracted using dichloromethane (DCM) from which DBU is removed by washing with dil. HCl. The crude product is purified by column chromatography on silica gel (200−400 mesh) using DCM as the eluent to give 65% of **2**. ^{1}H NMR (400 MHz, $CDCl_3$) δ = 2.40 (m, 2H), 3.62 (t, 2H), 4.20 (t, 2H), 4.56 (s, 2H), 6.40 (s, 1H), 6.90 (s, 1H), 7.6 (s, 1H); ^{13}C NMR (100 MHz, $CDCl_3$) δ = 29.80, 31.90, 41.10, 67.50, 102.30, 111.34, 113.68, 120, 125, 149.00, 154, 157, 160; FT-IR (ν_{max}) = 1731, 1607, 1552, 1505, 1464, 1416, 1369, 1288, 1208, 1152, 1206, 1152, 1036, 909, 871, 771, 724, 602, 534 cm^{-1}; MALDI-TOF ($C_{13}H_{11}BrCl_2O_3$), m/z = 365.

Synthesis of 3. An suspension of **1** (1.5 g, 6.25 mmol) in ethanol is added to a mixture of biotin (1 g, 4.08 mmol) and DBU (700 μL, 4.69 mmol) in dry ethanol and the mixture is heated to reflux for 4 h. **3** is precipitated by the addition of hexane. The crude product is purified by column chromatography on silica gel (200−400 mesh) using 2% methanol in ethylacetate as the eluent to give 50% of **3**. ^{1}H NMR (400 MHz, DMSO-d_6) δ = 1.36 (m, 2H), 1.60 (m, 4H), 2.46 (t, 2H), 2.80 (d, 1H), 2.84 (d, 1H), 3.08 (m, 1H), 4.13 (m, 1H), 4.29 (m, 1H), 5.36 (s, 2H), 6.23 (s, 1H), 6.36 (s, 1H), 6.42 (s, 1H), 6.93 (s, 1H), 7.75 (s, 1H); ^{13}C NMR (100 MHz, DMSO-d_6) δ = 25, 28.54, 33.45, 43.33, 55.20, 59.42, 62.22, 74.20, 92.88, 104.32, 110.60, 117.66, 125.38, 150.64, 154.15, 157.66, 161.87, 163.98, 173.80; FT-IR (ν_{max}) = 3230, 3059, 2932, 1714, 1600, 1405, 1316, 1260, 1162, 1032, 952, 876, 838, 700, 554 cm^{-1}; MALDI-TOF ($C_{20}H_{21}N_2O_6ClS$), m/z= 453.

Synthesis of 4. A mixture of biotin (1 g, 4.08 mmol), 1,3-dibromopropane (1.3 mL, 12.86 mmol) and DBU (1.85 mL, 12.40 mmol) dissolved in acetonitrile (100 mL) is heated to reflux for 3 h. **4** is precipitated from the reaction mixture by the addition of hexane (10 mL). The crude product is purified by column chromatography on silica gel (200−400 mesh) using DCM as the eluent to give 80% of **4**. ^{1}H NMR (400 MHz, $CDCl_3$) δ = 1. 46 (m, 2H), 1.70 (m, 4H), 2.18 (m, 2H), 2.35 (t, 2H), 2.74 (m, 1H), 2.94 (m, 1H), 3.16 (m, 1H), 3.47 (t, 2H), 4.21 (t, 2H), 4.34 (m, 1H), 4.56 (m, 1H), 5.16 (s, 1H), 5.56 (s, 1H); ^{13}C NMR (100 MHz, $CDCl_3$) δ = 29, 32.5, 34, 36, 38, 45, 53, 59, 64.5, 66.5, 101, 167, 178; FT-IR (ν_{max}) = 3241, 2941, 2843, 1736, 1474, 1418, 1362, 1324, 1262, 1223, 1195, 1115, 994, 859, 752, 728, 662, 624, 569, 544 cm^{-1}; MALDI-TOF ($C_{13}H_{21}N_2O_3BrS$), m/z= 365.

Synthesis of 5 from 2. A mixture of **2** (1 g, 2.75 mmol), biotin (2 g, 8.2 mmol) and K_2CO_3 (1.2 g, 8.28 mmol) is suspended in DMF and refluxed for 1 h. Unreacted biotin and K_2CO_3 in the reaction mixture are precipitated by the addition of chloroform. Finally, **5** is precipitated out by the addition of ice-cold water. The crude product is copiously washed with water and dried in a vacuum desiccator to give~ 30% of the desired product.

Synthesis of 5 from 3 and 4. A mixture of **3** (1 g, 2.20 mmol), **4** (0.9 g, 2.47 mmol) and K_2CO_3 (1 g, 7.7 mmol) is suspended in DMF and refluxed for 6 h. The residue is filtered-off and the product is precipitated from the filtrate by the addition of ice-cold water. The crude product is copiously washed with ice-cold water and dried in a vacuum desiccator to give~ 50% of the desired product. ^{1}H NMR (400 MHz, DMSO-d_6) δ= 1.36 (m, 4H), 1.63, (m, 8H), 2.11 (m, 2H), 2.31 (t, 2H), 2.46 (m, 2H), 2.59 (m, 2H), 2.81 (m, 2H), 3.07 (m, 2H), 3.30 (t, 2H), 4.13 (m, 2H), 4.23 (t, 2H), 4.3 (m, 2H), 5.36 (s, 2H), 6.32 (s, 1H), 6.35 (s, 1H), 6.40 (s, 1H), 6.43 (s, 1H), 7.24 (s, 1H), 7.82 (s, 1H), 8.23 (s, 1H); ^{13}C NMR (100 MHz, DMSO-d_6) δ = 25, 28, 33.6, 56, 60, 61.6, 67, 103, 118.7, 126, 144, 150.1, 154, 157, 160, 163, 173, 177; FT-IR (ν_{max}) = 3248, 3091, 2920, 2848, 2365, 3091, 1737, 1694, 1612, 1550, 1507, 1464, 1414, 1386, 1336, 1279, 1205, 1165, 1065, 887, 772, 734, 689, 602, 545; MALDI-TOF ($C_{33}H_{41}ClN_4O_9S_2$), m/z = 737. ^{1}H and ^{13}C NMR, MALDI-TOF MS, and FT-IR spectra of **1**−**5** are given in the Supporting Information.

Preparation of PUNP. Fabrication of PUNP involves two steps. In the first step, one of the biotin moieties in **5** is conjugated to streptavidin-functionalized Fe_3O_4 NPs by the addition of a 200 nM aqueous solution (50 μL) of streptavidin-functionalized

Fe_3O_4 NPs to a 20 μM solution of **5** in DMSO (50 μL). This mixture is incubated at 37 °C for 2 h, and the excess ligand is removed by dialysis against a membrane for 2 kDa. In the second step, biotin-functionalized Fe_3O_4 NP prepared in the first step is conjugated with streptavidin-functionalized CdSe/ZnS QDs. Here, 50 μL of biotin-functionalized Fe_3O_4 NP (100 nM) is added in five portions to a QD solution (50 μL, 1 μM) and incubated at 37 °C for 2 h. This incubation resulted in the formation of PUNP in which *ca.* 10 QDs are conjugated to each Fe_3O_4 NP through the photouncaging ligand **5**.

Preparation of PUNP—Allatostatin Conjugate. Lyophilized allatostatin (Genscript Corporation) reconstituted into a 0.75 mM solution in sterile-filtered water is biotinylated using a 15 mM aqueous solution of biotin-3-sulfo-NHS ester at 25 °C for 1 h. Biotinylated allatostatin is purified by gel filtration on a sephadex G-25 column (Sigma), diluted with sterile filtered water into a 250 nM (100 μL) solution, and added to a 50 nM aqueous solution (100 μL) of PUNP. This mixture when reacted at 25 °C for 30 min provided the PUNP—allatostatin conjugate.

Cytotoxicity Assay. Cytotoxicity of CdSe/ZnS QD, Fe_3O_4 NP, **3**, **5**, PUNP and photouncaged products is evaluated by 3-(4,5-dimethylthiazole-2-yl)-2,5-diphenyltetrazolium chloride (MTT) assay using an MTT cell proliferation kit (Roche Diagnostics). Here, *ca.* 1×10^6 human epithelial lung adenocarcinoma cells (H1650) are inoculated per plate into 96-well tissue culture plates (FALCON) containing DMEM supplemented with 10% FBS, and incubated for 48 h at 37 °C. The cells are then washed with PBS and the medium is exchanged with DMEM without FBS. The cells are supplemented with different concentrations of coumarinylmethyl alcohol (0.1, 1, and 10 μM), **3** (0.01, 0.1, and 1 μM), **5** (0.01, 0.1, and 1 μM), Fe_3O_4 NP (1, 10, and 100 nM), CdSe/ZnS QD (0.1, 1, and 10 nM), or PUNP (0.1, 1, and 10 nM). After 24 h incubation, the cells are washed three times with PBS and subsequently treated with MTT solution (10 μL, 5 mg/mL) for 4 h. The treated cells are lysed by adding 10% SDS in 0.01 M HCl (100 μL/well), and the formazan crystals formed as a result of the reduction of MTT by the mitochondrial reductase enzyme are dissolved overnight at 37 °C. The absorbance of formazan is determined at 550 nm in a microplate reader and the cell viability is obtained by comparing the absorbance of formazan produced by the treated cells with that by control cells.

Conflict of Interest: The authors declare no competing financial interest.

Supporting Information Available: Figure S1, UV—vis absorption of **3**, **5**, Fe_3O_4 NP, QD and PUNP, and photoluminescence spectra of **3**, **5**, QD and PUNP; Figure S2, XPS spectra of PUNP; Figure S3, time-dependent UV-Vis absorption spectra of **5** under 340 nm light from a Xe lamp; Figure S4, large area fluorescence images of B16 cells treated with PUNP—allatostatin conjugate; Figure S5, MTT assay histograms for H1650 cells treated with **3**, **5** and the photoproducts of **3**; Figure S6, ^1H and ^{13}C NMR spectra of **1**—**5**; Figure S7, mass spectra of **1**—**5**; Figure S8, FTIR spectra of **1**—**5**. This material is available free of charge *via* the Internet at http://pubs.acs.org.

Acknowledgment. We thank Dr. Shohei Yamamura of AIST for providing H1650 cells, Dr. Akinari Sonoda of AIST for his support in the measurements of NMR and FTIR spectra, and Dr. D. Sakthikumar of Toyo University for XPS measurements. This work is carried out under the Precursory Research for Embryonic Science and Technology (PRESTO) program of Japan Science and Technology Agency (JST).

REFERENCES AND NOTES

1. Cheon, J.; Lee, J. H. Synergistically Integrated Nanoparticles as Multimodal Probes for Nanobiotechnology. *Acc. Chem. Res.* **2008**, *41*, 1630–1640.
2. Wang, B.; Hai, J.; Wang, Q.; Li, T.; Yang, Z. Coupling of Luminescent Terbium Complexes to Fe_3O_4 Nanoparticles for Imaging Applications. *Angew. Chem., Int. Ed.* **2011**, *50*, 3063–3066.
3. Shi, D.; Cho, H. S.; Chen, Y.; Xu, H.; Gu, H.; Lian, J.; Wang, W.; Liu, G.; Huth, C.; Wang, L.; *et al.* Fluorescent Polystyrene-Fe_3O_4 Composite Nanospheres for *In vivo* Imaging and Hyperthermia. *Adv. Mater.* **2009**, *21*, 2170–2173.
4. Chen, F.; Zhang, S.; Bu, W.; Chen, Y.; Xiao, Q.; Liu, J.; Xing, H.; Zhou, L.; Peng, W.; Shi, J. A Uniform Sub-50 nm-Sized Magnetic/Upconversion Fluorescent Bimodal Imaging Agent Capable of Generating Singlet Oxygen by using a 980 nm Laser. *Chem.—Eur. J.* **2012**, 7082–7090.
5. Wang, G.; Su, X. A Novel Technology for the Detection, Enrichment, and Separation of Trace Amounts of Target DNA Based on Amino-Modified Fluorescent Magnetic Composite Nanoparticles. *Anal. Bioanal. Chem.* **2010**, *397*, 1251–1258.
6. Tseng, P.; Di Carlo, D.; Judy, J. W. Rapid and Dynamic Intracellular Patterning of Cell-Internalized Magnetic Fluorescent Nanoparticles. *Nano Lett.* **2009**, *9*, 3053–3059.
7. Song, E.-Q.; Hu, J.; Wen, C.-Y.; Tian, Z.-Q.; Yu, X.; Zhang, Z.-L.; Shi, Y.-B.; Pang, D.-W. Fluorescent-Magnetic-Biotargeting Multifunctional Nanobioprobes for Detecting and Isolating Multiple Types of Tumor Cells. *ACS Nano* **2011**, *5*, 761–770.
8. Lee, J. H.; Lee, K.; Moon, S. H.; Lee, Y.; Park, T. G.; Cheon, J. All-in-One Target-Cell-Specific Magnetic Nanoparticles for Simultaneous Molecular Imaging and siRNA Delivery. *Angew. Chem., Int. Ed.* **2009**, *48*, 4174–4179.
9. Liong, M.; Lu, J.; Kovochich, M.; Xia, T.; Ruehm, S. G.; Nel, A. E.; Tamanoi, F.; Zink, J. I. Multifunctional Inorganic Nanoparticles for Imaging, Targeting, and Drug Delivery. *ACS Nano* **2008**, *2*, 889–896.
10. Fernández, B.; Gálvez, N.; Cuesta, R.; Hungría, A. B.; Calvino, J. J.; Domínguez-Vera, J. M. Quantum Dots Decorated with Magnetic Bionanoparticles. *Adv. Funct. Mater.* **2008**, *18*, 3931–3935.
11. Stasiuk, G. J.; Tamang, S.; Imbert, D.; Poillot, C.; Giardiello, M.; Tisseyre, C.; Barbier, E. L.; Fries, P. H.; de Waard, M.; Reiss, P.; Mazzanti, M. Cell-Permeable Ln(III) Chelate-Functionalized InP Quantum Dots as Multimodal Imaging Agents. *ACS Nano* **2011**, *5*, 8193–8201.
12. Kim, H. M.; Lee, H.; Hong, K. S.; Cho, M. Y.; Sung, M. -H.; Poo, H.; Lim, Y. T. Synthesis and High Performance of Magnetofluorescent Polyelectrolyte Nanocomposites as MR/Near-Infrared Multimodal Cellular Imaging Nanoprobes. *ACS Nano* **2011**, *5*, 8230–8240.
13. Zhang, F.; Shi, Q.; Zhang, Y.; Shi, Y.; Ding, K.; Zhao, D.; Stucky, G. D. Fluorescence Upconversion Microbarcodes for Multiplexed Biological Detection: Nucleic Acid Encoding. *Adv. Mater.* **2011**, *23*, 3775–3779.
14. Park, Y. I.; Kim, J. H.; Lee, K. T.; Jeon, K.-S.; Na, H. B.; Yu, J. H.; Kim, H. M.; Lee, N.; Choi, S. H.; Baik, S.-I.; *et al.* Nonblinking and Nonbleaching Upconverting Nanoparticles as an Optical Imaging Nanoprobe and T1Magnetic Resonance Imaging Contrast Agent. *Adv. Mater.* **2009**, *21*, 4467–4471.
15. Medintz, I. L.; Uyeda, H. T.; Goldman, E. R.; Mattoussi, H. Quantum Dot Bioconjugates for Imaging, Labelling and Sensing. *Nat. Mater.* **2005**, *4*, 435–446.
16. Biju, V.; Itoh, T.; Anas, A.; Sujith, A.; Ishikawa, M. Semiconductor Quantum Dots and Metal Nanoparticles: Syntheses, Optical Properties, and Biological Applications. *Anal. Bioanal. Chem.* **2008**, *391*, 2469–2495.
17. Biju, V.; Anas, A.; Akita, H.; Shibu, E. S.; Itoh, T.; Harashima, H.; Ishikawa, M. FRET from Quantum Dots to Photodecompose Undesired Acceptors and Report the Condensation and Decondensation of Plasmid DNA. *ACS Nano* **2012**, *6*, 3776–3788.
18. Howes, P.; Green, M.; Bowers, A.; Parker, D.; Varma, G.; Kallumadil, M.; Hughes, M.; Warley, A.; Brain, A.; Botnar, R. Magnetic Conjugated Polymer Nanoparticles as Bimodal Imaging Agents. *J. Am. Chem. Soc.* **2010**, *132*, 9833–9842.
19. Gao, J.; Zhang, B.; Gao, Y.; Pan, Y.; Zhang, X.; Xu, B. Fluorescent Magnetic Nanocrystals by Sequential Addition of Reagents in a One-Pot Reaction: A Simple Preparation for Multifunctional Nanostructures. *J. Am. Chem. Soc.* **2007**, *129*, 11928–11935.
20. Kim, H.; Achermann, M.; Balet, L. P.; Hollingsworth, J. A.; Klimov, V. I. Synthesis and Characterization of Co/CdSe Core/Shell Nanocomposites: Bifunctional Magnetic-Optical Nanocrystals. *J. Am. Chem. Soc.* **2005**, *127*, 544–546.

21. Yoon, T.-J.; Kim, J.-S.; Kim, B. G.; Yu, K. N.; Cho, M.-H.; Lee, J. -K. Multifunctional Nanoparticles Possessing a "Magnetic Motor Effect" for Drug or Gene Delivery. *Angew. Chem., Int. Ed.* **2005**, *44*, 1068–1071.
22. Cambridge, S. B. Drosophila Mitotic Domain Boundaries as Cell Fate Boundaries. *Science* **1997**, *277*, 825–828.
23. Neveu, P.; Aujard, I.; Benbrahim, C.; Le Saux, T.; Allemand, J.-F.; Vriz, S.; Bensimon, D.; Jullien, L. A Caged Retinoic Acid for One- and Two-Photon Excitation in Zebrafish Embryos. *Angew. Chem., Int. Ed.* **2008**, *47*, 3744–3746.
24. Mayer, G.; Heckel, A. Biologically Active Molecules with a "Light Switch.. *Angew. Chem., Int. Ed.* **2006**, *45*, 4900–4921.
25. Hagen, V.; Kilic, F.; Schaal, J.; Dekowski, B.; Schmidt, R.; Kotzur, N. [8-[Bis(carboxymethyl)aminomethyl]-6-bromo-7-hydroxycoumarin-4-yl]methyl Moieties as Photoremovable Protecting Groups for Compounds with COOH, NH_2, OH, and C═O Functions. *J. Org. Chem.* **2010**, *75*, 2790–2797.
26. Lin, Q.; Bao, C.; Cheng, S.; Yang, Y.; Ji, W.; Zhu, L. Target-Activated Coumarin Phototriggers Specifically Switch on Fluorescence and Photocleavage Upon Bonding to Thiol-Bearing Protein. *J. Am. Chem. Soc.* **2012**, *134*, 5052–5055.
27. Hagen, V.; Dekowski, B.; Nache, V.; Schmidt, R.; Geißler, D.; Lorenz, D.; Eichhorst, J.; Keller, S.; Kaneko, H.; Benndorf, K.; *et al.* Coumarinylmethyl Esters for Ultrafast Release of High Concentrations of Cyclic Nucleotides Upon One- and Two-Photon Photolysis. *Angew. Chem., Int. Ed.* **2005**, *44*, 7887–7891.
28. Gu, H.; Zheng, R.; Zhang, X.; Xu, B. Facile One-Pot Synthesis of Bifunctional Heterodimers of Nanoparticles: A Conjugate of Quantum Dot and Magnetic Nanoparticles. *J. Am. Chem. Soc.* **2004**, *126*, 5664–5665.
29. Shi, W.; Zeng, H.; Sahoo, Y.; Ohulchanskyy, T. Y.; Ding, Y.; Wang, Z. L.; Swihart, M.; Prasad, P. N. A General Approach to Binary and Ternary Hybrid Nanocrystals. *Nano Lett.* **2006**, *6*, 875–881.
30. Lu, H.; Yi, G.; Zhao, S.; Chen, D.; Guo, L.-H.; Cheng, J. Synthesis and Characterization of Multifunctional Nanoparticles Possessing Magnetic, Up-Conversion Fluorescence and Bio- affinity Properties. *J. Mater. Chem.* **2004**, *14*, 1336.
31. Pöselt, E.; Schmidtke, C.; Fischer, S.; Peldschus, K.; Salamon, J.; Kloust, H.; Tran, H.; Pietsch, A.; Heine, M.; Adam, G.; *et al.* Tailor-Made Quantum Dot and Iron Oxide Based Contrast Agents for *in Vitro* and *in Vivo* Tumor Imaging. *ACS Nano* **2012**, *6*, 3346–3355.
32. Kim, J. S.; Rieter, W. J.; Taylor, K. M. L.; An, H.; Lin, W.; Lin, W. Self-Assembled Hybrid Nanoparticles for Cancer-Specific Multimodal Imaging. *J. Am. Chem. Soc.* **2007**, *129*, 8962–8963.
33. Salgueiriño-Maceira, V.; Correa-Duarte, M. A.; Spasova, M.; Liz-Marzán, L. M.; Farle, M. Composite Silica Spheres with Magnetic and Luminescent Functionalities. *Adv. Funct. Mater.* **2006**, *16*, 509–514.
34. Selvan, S. T.; Patra, P. K.; Ang, C. Y.; Ying, J. Y. Synthesis of Silica-Coated Semiconductor and Magnetic Quantum Dots and their use in the Imaging of Live Cells. *Angew. Chem., Int. Ed.* **2007**, *46*, 2448–2452.
35. Kim, J.; Lee, J. E.; Lee, J.; Yu, J. H.; Kim, B. C.; An, K.; Hwang, Y.; Shin, C.-H.; Park, J.-G.; Kim, J.; *et al.* Magnetic Fluorescent Delivery Vehicle using Uniform Mesoporous Silica Spheres Embedded with Monodisperse Magnetic and Semiconductor Nanocrystals. *J. Am. Chem. Soc.* **2006**, *128*, 688–689.
36. Lee, J. H.; Schneider, B.; Jordan, E. K.; Liu, W.; Frank, J. A. Synthesis of Complexable Fluorescent Superparamagnetic Iron Oxide Nanoparticles and Cell Labeling for Clinical Application. *Adv. Mater.* **2008**, *20*, 2512–2516.
37. Bridot, J. -L.; Faure, A. -C.; Laurent, S.; Rivière, C.; Billotey, C.; Hiba, B.; Janier, M.; Josserand, V.; Coll, J.-L.; Vander Elst, L.; *et al.* Hybrid Gadolinium Oxide Nanoparticles: Multimodal Contrast Agents for *in Vivo* Imaging. *J. Am. Chem. Soc.* **2007**, *129*, 5076–5084.
38. Fan, H.-M.; Olivo, M.; Shuter, B.; Yi, J.-B.; Bhuvaneswari, R.; Tan, H. R.; Xing, G.-C.; Ng, C.-T.; Liu, L.; Lucky, S. S.; *et al.* Quantum Dot Capped Magnetite Nanorings as High Performance Nanoprobe for Multiphoton Fluorescence and Magnetic Resonance Imaging. *J. Am. Chem. Soc.* **2010**, *132*, 14803–14811.
39. Jie, G.; Yuan, J. Novel Magnetic Fe_3O_4@CdSe Composite Quantum Dot-Based Electrochemiluminescence Detection of Thrombin by a Multiple DNA Cycle Amplification Strategy. *Anal. Chem.* **2012**, *84*, 2811–2817.
40. Gao, J.; Zhang, W.; Huang, P.; Zhang, B.; Zhang, X.; Xu, B. Intracellular Spatial Control of Fluorescent Magnetic Nanoparticles. *J. Am. Chem. Soc.* **2008**, *130*, 3710–3711.
41. Santra, S.; Yang, H.; Holloway, P. H.; Stanley, J. T.; Mericle, R. A. Synthesis of Water-Dispersible Fluorescent, Radio-Opaque, and Paramagnetic CdS:Mn/ZnS Quantum Dots: A Multifunctional Probe for Bioimaging. *J. Am. Chem. Soc.* **2005**, *127*, 1656–1657.
42. Biju, V. Chemical Modifications and Bioconjugate Reactions of Nanomaterials for Sensing, Imaging, Drug Delivery and Therapy. *Chem. Soc. Rev.* **2013**, *42*, DOI:10.1039/C3CS60273G.
43. Cho, B. R.; Son, K. H.; Lee, S. H.; Song, Y.-S.; Lee, Y.-K.; Jeon, S.-J.; Choi, J. H.; Lee, H.; Cho, M. Two Photon Absorption Properties of 1,3,5-Tricyano-2,4,6-tris(styryl)benzene Derivatives. *J. Am. Chem. Soc.* **2001**, *123*, 10039–10045.
44. Makarov, N. S.; Drobizhev, M.; Rebane, A. Two-Photon Absorption Standards in the 550−1600 nm Excitation Wavelength Range. *Opt. Express* **2008**, *16*, 4029–4047.
45. Biju, V.; Itoh, T.; Ishikawa, M. Delivering Quantum Dots to Cells: Bioconjugated Quantum Dots for Targeted and Nonspecific Extracellular and Intracellular Imaging. *Chem. Soc. Rev.* **2010**, *39*, 3031–3056.
46. Anas, A.; Okuda, T.; Kawashima, N.; Nakayama, K.; Itoh, T.; Ishikawa, M.; Biju, V. Clathrin-Mediated Endocytosis of Quantum Dot-Peptide Conjugates in Living Cells. *ACS Nano* **2009**, *3*, 2419–2429.
47. Biju, V.; Muraleedharan, D.; Nakayama, K.; Shinohara, Y.; Itoh, T.; Baba, Y.; Ishikawa, M. Quantum Dot-Insect Neuropeptide Conjugates for Fluorescence Imaging, Transfection, and Nucleus Targeting of Living Cells. *Langmuir* **2007**, *23*, 10254–10261.
48. Yang, Y.; Zhao, Q.; Feng, W.; Li, F. Luminescent Chemodosimeters for Bioimaging. *Chem. Rev.* **2013**, *113*, 192–270.
49. Shibu, E. S.; Sugino, S.; Ono, K.; Saito, H.; Nishioka, A.; Yamamura, S.; Sawada, M.; Nosaka, Y.; Biju, V. Singlet-Oxygen-Sensitizing Near-Infrared-Fluorescent Multimodal Nanoparticles. *Angew. Chem., Int. Ed.* **2013**, *52*, 10559–10563.
50. Shao, Q.; Xing, B. Photoactive Molecules for Applications in Molecular Imaging and Cell Biology. *Chem. Soc. Rev.* **2010**, *39*, 2835–2846.
51. Shibu, E. S.; Hamada, M.; Murase, N.; Biju, V. Nanomaterials Formulations for Photothermal and Photodynamic Therapy of Cancer. *J. Photochem. Photobiol., C* **2013**, *15*, 53–72.
52. Yang, Y.; Shao, Q.; Deng, R.; Wang, C.; Teng, X.; Cheng, K.; Cheng, Z.; Huang, L.; Liu, Z.; Liu, X.; Xing, B. *In Vitro* and *in Vivo* Uncaging and Bioluminescence Imaging by using Photocaged Upconversion Nanoparticles. *Angew. Chem., Int. Ed.* **2012**, *51*, 3125–3129.